Atomic-level growth study of vanadium oxide nanostructures on Rh(111)

J. Schoiswohl, M. Sock, S. Eck, S. Surnev,* M. G. Ramsey, and F. P. Netzer

Institut für Experimentalphysik, Karl-Franzens-Universität Graz, A-8010 Graz, Austria

G. Kresse

Institut für Materialphysik, Universität Wien, A-1090 Wien, Austria

The growth and structure of ultrathin vanadium oxide films on Rh(111) has been studied by scanning tunneling microscopy, low-energy electron diffraction, high-resolution x-ray photoelectron spectroscopy, high-resolution electron energy-loss spectroscopy, and *ab initio* density-functional-theory calculations. For sub-monolayer coverages [$\Theta < 0.6$ MLE (monolayer equivalents)], depending on the oxide preparation route (reactive evaporation vs postoxidation), two well-ordered V-oxide phases with $(\sqrt{7} \times \sqrt{7})R19.1°$ and $(\sqrt{13} \times \sqrt{13})R13.8°$ structures and similar electronic and vibrational signatures have been observed. The $\sqrt{7}$ and $\sqrt{13}$ phases are interface stabilized and exhibit high formal oxidation states ($\sim 5^+$). In the oxide coverage range $0.6 < \Theta < 1.2$ MLE, i.e., after the completion of the first oxide layer, the $\sqrt{7}$ and $\sqrt{13}$ structures are replaced by several coexisting V-oxide phases, where the oxidation state of the V atoms progressively decreases from 4^+ to 2^+ with increasing oxide coverage. For coverages exceeding 2 MLE a bulk-type V_2O_3 phase with corundum structure grows epitaxially on the Rh(111) surface. The observed growth mode is examined by assessing kinetic and energetic effects in the ultrathin oxide film growth. The importance of the oxide-free areas of the metal support for the formation of highly oxidized V-oxide layers at the initial stages of growth is discussed.

I. INTRODUCTION

Ultrathin layers of oxide materials have applications in many areas of advanced technology, such as in form of barrier layers in novel magnetoelectronic tunneling junctions, as dielectric layers in gas sensing devices, as protective layers in anticorrosion coatings, and as supports in the field of heterogeneous catalysis.[1,2] On a fundamental scientific level it is of interest to what extent the properties of ultrathin layers of oxides in nanometer dimensions resemble those of the respective bulk materials. Due to the spatial confinement and the relative importance of the interfaces to substrate and other adjacent materials, thin films with the thickness of the order of a few unit cells may have completely different and novel physical and chemical properties than their respective bulk counterparts. The study of oxides in ''nanolayer'' phases is therefore an important scientific endeavor on the way to the emerging nanotechnologies of the upcoming decades.

In previous work we have studied the growth and structure of ultrathin films of vanadium oxides on Pd(111) single-crystal surfaces.[3–6] It was found that in the ultrathin film limit the structures of the V-oxide phases on Pd(111) bear little resemblance to the known bulk vanadium oxide structures, and many novel and metastable, with respect to further growth, oxide phases have been detected. These structures derive their (meta)stability partly from the specific bonding interactions to the Pd substrate, and partly from their quasi-two-dimensional character with a favorable balance of interfacial strain and interlayer bonding energies. In this context it is of interest to examine the influence of the geometry and the chemistry of the substrate surface on the structure of the growing oxide film. The Rh(111) surface has a unit-cell lattice constant $d = 2.69$ Å, which is very close to that of the Pd(111) surface ($d = 2.75$ Å). However, the chemistry of Rh atoms is different from Pd, in particular, in what concerns the affinity to chemisorbed oxygen, which is stronger on Rh(111).[7] This is reflected in a higher desorption temperature[8] and also in the amount of subsurface oxygen under given conditions, which is smaller on Rh(111) than on Pd(111).[9] The different affinity of the substrate to oxygen may be of importance for the formation of the first oxide monolayer, because the preparation of ordered oxide phases requires the presence of gas phase oxygen at elevated substrate temperatures.

In the present work we have investigated the growth and structures of ultrathin vanadium oxide layers on Rh(111) surfaces, using variable-temperature scanning tunneling microscopy (STM) to reveal the growth morphology and the atomic-level structures of the oxide phases. The STM results have been supplemented by low-energy electron diffraction (LEED) and high-resolution electron energy loss spectroscopy (HREELS) observations to assist with the structure determinations, and by photoelectron spectroscopy of valence and core levels to specify the oxidation state and the stoichiometries of the oxide phases. As on Pd(111) the phase diagram of vanadium oxides on Rh(111) displays a pronounced polymorphic behavior, with many oxide structures in the low coverage regime [< 2 monolayers (ML)]. However, these oxide phases have not only novel structures with respect to bulk vanadium oxides, but also with respect to those found on Pd(111). This is an interesting observation and clearly demonstrates the influence of the substrate chemistry. There are, however, some general similarities in the V-oxide growth pattern on Pd and Rh surfaces, which will also be discussed here. For coverages > 2 ML the vanadium oxide

layers converge irrespective of the substrate material to bulk-type V_2O_3, which is the stable vanadium oxide phase under the conditions employed in this study.

II. EXPERIMENTAL AND COMPUTATIONAL PROCEDURES

A. Experiment

The experiments were performed in three different custom-designed ultrahigh-vacuum (UHV) systems, operating at base pressures $p < 1 \times 10^{-10}$ mbar. The STM and HREELS measurements have been performed in Graz, in two custom-designed UHV systems. The STM system is equipped with a variable-temperature STM (Oxford Instruments), LEED, Auger electron spectroscopy (AES), and crystal cleaning facilities.[3] The STM images were recorded in a constant current mode at room temperature. Electrochemically etched W tips cleaned *in situ* by electron bombardment were used. Tunneling currents as low as 50 pA were employed in order to minimize the influence of the tip on the oxide structures. The HREELS measurements were performed with an ErEELS 31 spectrometer, as described elsewhere.[10] The HREELS spectra were taken at room temperature with a primary energy of 5.5 eV in specular reflection geometry $\Theta_{in} = \Theta_{out} = 60°$, with a typical resolution of ~ 3.5 meV as measured at the full width at half maximum of the reflected primary peak.

High-resolution photoemission measurements with use of synchrotron radiation were carried out at beamline I311 in the Swedish synchrotron radiation laboratory MAX-lab in Lund.[11] The experimental end station consists of separate analyzer and preparation chambers in a vertical mount, separated with a gate valve. The system is equipped with a large hemispherical electron energy analyzer (Scienta SES 200). A photon energy of 620 eV has been used for exciting electrons from the V $2p$ and O $1s$ core levels, whereas valence-band spectra have been measured with a photon energy of 110 eV. The corresponding experimental resolution was better than 250 meV at $h\nu = 620$ eV and 100 meV at $h\nu = 110$ eV. The core-level and valence-band spectra were measured at room temperature and at normal emission. The binding-energy scale was calibrated with respect to the Fermi energy of the crystal in each case. The core-level spectra were normalized to the secondary electron background at a few eV lower binding energy than the respective core-level peak. The V $2p_{3/2}$ spectra were analyzed by peak decomposition using Donjiac-Šunjic line shapes[12] convoluted with Gaussians after subtracting a Shirley background from the experimental data.

Clean Rh(111) surfaces were prepared by 1.5 keV Ar$^+$-ion sputtering, followed by annealing to ~ 830 °C for several minutes, and by heating cycles in O_2 followed by a final short flash to 800 °C . The cleanliness of the Rh(111) sample was checked by AES or by measuring valence-band spectra at photon energies close to the Cooper minimum of the Rh $4d$ photoionization cross section (110 eV). LEED was used to control the preparation of the respective oxide surface structures in the different experimental systems.

Vanadium oxide films were prepared either by reactive evaporation of V metal onto the clean Rh(111) surface at elevated substrate temperature, or by postoxidation of V metal deposited onto the Rh(111) crystal at room temperature and subsequent oxidation. For the reactive evaporation procedure the sample was heated to 250 °C or 400 °C in 2×10^{-7} mbar O_2 and after the deposition the sample was kept at these conditions for additional 5 min; finally it was cooled down to $T < 100$ °C in the oxygen atmosphere to prevent the thermal reduction of the oxide layer. For the postoxidation procedure vanadium was deposited on the Rh(111) surface at room temperature and was subsequently annealed to 400 °C in 2×10^{-7} mbar O_2 for 5 min and cooled down in oxygen atmosphere. The vanadium deposition rate was monitored by a quartz crystal microbalance and was varied between 0.2 ML/min for low V coverages (below 1.5 ML) and 0.5 ML/min for higher coverages. The V-oxide coverage will be given in *monolayer equivalents* (MLE), where 1 MLE contains the same number of V atoms as 1 ML of Rh(111) atoms.

B. Computational

The density-functional calculations were performed using the Vienna *ab initio* simulation package.[13] The interaction between the valence electrons and ionic cores was described by the projector augmented wave method in the implementation of Kresse and Joubert,[14] and the plane-wave cutoff was set to 250 eV. Generalized gradient corrections were applied throughout this work.[15] Generally four-layer thick slabs and k-point grids corresponding to 8×8 points in the Brillouin zone of the primitive surface cell were used. The precise calculational setup was already described in a number of papers and is therefore not repeated here; for details, in particular on the construction of surface phase diagrams, we refer to Ref. 16. The vibrational spectra of the considered surface oxides were calculated using finite differences. Each atom in the oxide was displaced by 0.02 Å in each direction. From this calculation the interatomic force constants were determined, and the mass weighted force-constant matrix was diagonalized. This yields the vibrational frequencies and the vibrational eigenmodes of the entire slab. The intensities of the vibrational loss peaks in the HREELS spectra were calculated by determining the derivative of the square of the dipole with respect to each vibrational mode (the dynamic dipole). The simulated STM images were calculated in the Tersoff-Hamann approximation,[17] with constant current topographs approximated by isosurfaces of constant charge. Typically the images were evaluated at zero bias 3–4 Å above the topmost atom.

III. RESULTS

A. Growth morphology—overview

The growth morphology of vanadium oxide overlayers on Rh(111) deposited by reactive evaporation at 250 °C substrate temperature is illustrated by the constant-current topographic STM images in Fig. 1. For low coverages ($\Theta = 0.13$ MLE) the oxide grows in a random island growth mode with irregularly shaped islands, and no preferential decoration of step edges is observed. At $\Theta \sim 0.35–0.4$ MLE
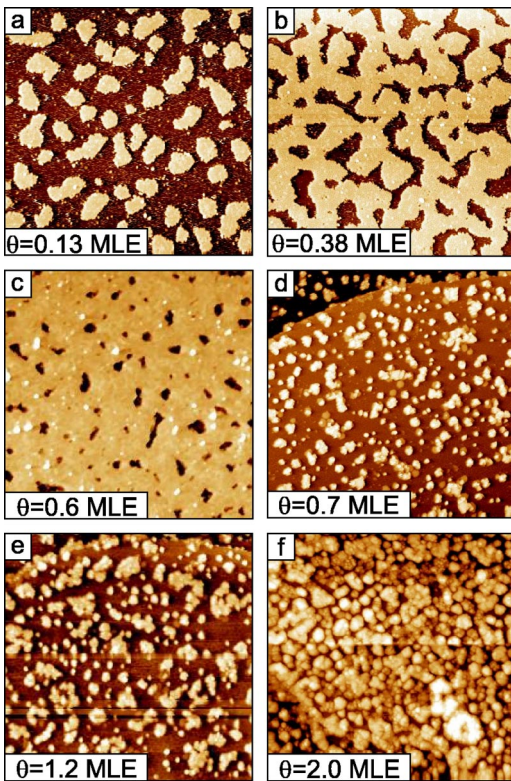
FIG. 1. Constant current topographic STM images of V-oxide films grown on Rh(111) at $T = 250$ °C substrate temperature and an oxygen pressure of 2×10^{-7} mbar. The coverages are indicated on the images. All images are 1000×1000 Å^2 area scans with sample voltage $U = 2$ V and tunneling current $I = 0.1$ nA.

FIG. 2. Series of STM images (1000×1000 Å^2, $U = 2.0$ V, $I = 0.1$ nA) of V-oxide films grown on Rh(111) at $T = 400$ °C substrate temperature and an oxygen pressure of 2×10^{-7} mbar. Coverages are indicated on the images.

a percolation threshold is reached [Fig. 1(b)], while the first oxide monolayer is almost completed at $\Theta = 0.6$ MLE [Fig. 1(c)]. In the coverage range 0.7–1.0 MLE the oxide overlayer displays a peculiar behavior, and a phase separation seems to take place: the first oxide monolayer becomes destabilized and transforms into two other phases. This is shown in Figs. 1(d) and 1(e), where one phase forms irregular shaped islands, while the other phase is in the areas in between and shows up with a darker contrast under the given STM imaging conditions (see Sec. III C for further discussion). For $\Theta \sim 2$ MLE the three-dimensional island growth prevails [Fig. 1(f)], with internally ordered islands that form small crystallites (see results presented in Sec. III D). This is typical for polycrystalline epitaxy,[18] which has also been observed for V-oxide films on Pd(111) (Ref. 5) under similar preparation conditions.

Figure 2 illustrates the vanadium oxide growth pattern at 400 °C substrate temperature. In general, better ordered and larger size islands are obtained. Figures 2(a) and 2(b) show STM images for submonolayer oxide coverages ($\Theta < 0.6$ MLE), where large islands decorate the Rh terraces and extend to the lower step edges [Fig. 2(b)], indicating the onset of a step flow mechanism at this temperature. Also at this substrate temperature a phase separation occurs upon completion of the first monolayer. This is evident from the STM images in Figs. 2(c) and 2(d). Here a phase with apparently hexagonal "tiles" nucleates at the upper and lower
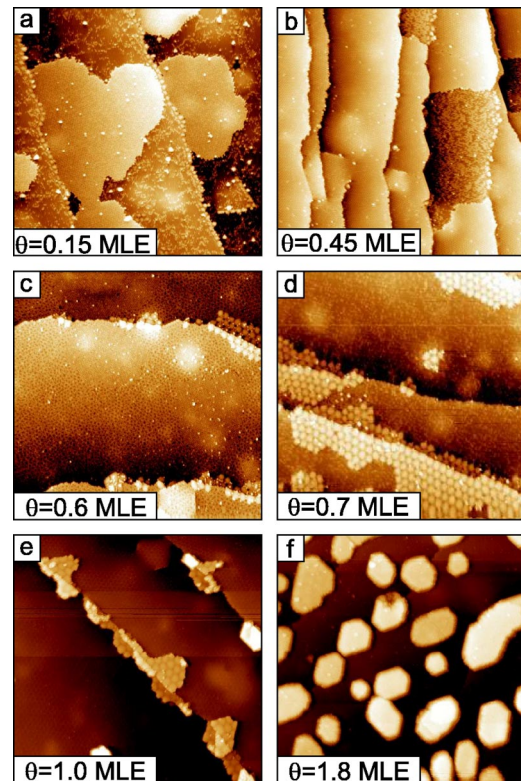
step edges, which increases in area from 0.6 to 0.7 MLE. Between the tile phase islands a poorly ordered flat oxide layer develops which is imaged with a darker contrast in the STM topographs. At $\Theta = 1.0$ MLE the hexagonal tile phase decreases again in area and the next layer nucleates on top (seen as brighter agglomerates). The oxide layer in between the "tile" phase islands has transformed at this point into a more compact and well-ordered wetting layer, which is shown in more detail in Sec. III C. At $\Theta = 1.8$ MLE hexagonally shaped three-dimensional flat islands with an average height of ~ 20 Å coexist with the wetting layer. For higher coverages the three-dimensional islands coalesce and form a well-ordered oxide film, as will be shown in Sec. III D [Figs. 11(c) and 11(d)].

Vanadium $2p_{3/2}$ core-level spectra for V-oxide growth at 250 °C are displayed as a function of oxide coverage in Fig. 3(a). The V $2p_{3/2}$ spectral lines are generally broad and their decomposition analysis for selected oxide phases will be presented below. Here we notice that for the first monolayer, i.e., for coverages up to 0.5–0.6 MLE, the V $2p$ peak maxima occur at a binding energy (BE) of ~ 515.5 eV, but then the peak splits into two components [indicated by the solid lines in Fig. 3(a)], with higher intensity developing at the lower BE side in the coverage range 0.6–1 MLE. This is the region of the phase separation, which is therefore also reflected in x-ray photoemission spectroscopy (XPS). The development of a low BE peak in the V $2p$ structure indicates that vanadium atoms in a lower oxidation state are
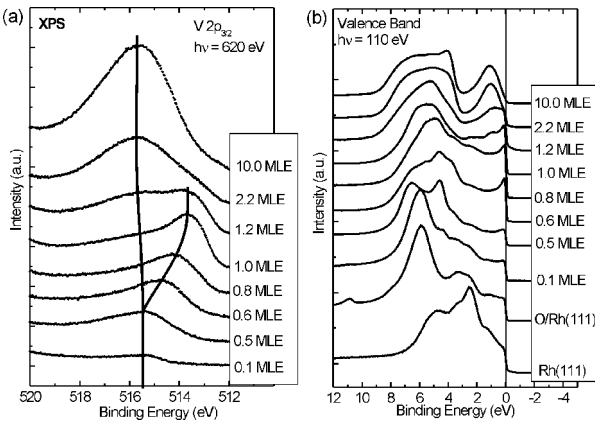
FIG. 3. (a) V $2p_{3/2}$ core-level spectra, excited with $h\nu = 620$ eV, as a function of oxide coverage. (b) Valence-band photoemission spectra excited with $h\nu = 110$ eV as a function of the oxide coverage. The spectra labeled Rh(111) and O/Rh(111) are from the clean substrate and the pristine Rh(111)-O(2×1) surface, respectively.

mainly present in this transition region. With increasing coverage the V $2p$ spectral weight shifts again to higher binding energy (see 1.2 MLE spectrum) and for coverages $\Theta > 2$ MLE the V $2p$ maxima converge to a binding energy of ~515.7 eV, which is characteristic of bulk-type V_2O_3.[19]

Figure 3(b) displays a sequence of valence-band spectra as a function of oxide coverage. The spectrum of the clean Rh(111) surface shows the emission from the Rh $4d$ valence-band states between the Fermi energy ($E_B = 0$) and ~7 eV binding energy. The presence of chemisorbed oxygen on the Rh(111) surface [spectrum O/Rh(111)] leads to the additional emission of photoelectrons from O $2p$ states at ~5–8 eV binding energy. With increasing oxide coverage the Rh $4d$ emission is quenched progressively by the oxide overlayer and the O $2p$ band of the oxide overlayer evolves between $E_B = 4$–8 eV. The O $2p$ band of the 0.5 MLE vanadium oxide surface shows two pronounced maxima at $E_B \sim 4.5$ and 7 eV. These emission structures change significantly in the coverage region 0.6–1.0 MLE, and a sharp peak develops at the Fermi energy. For higher oxide coverages, the peak at E_F shifts back to higher binding energy and gives way to a V $3d$ emission at $E_B \sim 1$ eV. The O $2p$ band also changes structure and the valence-band spectrum becomes characteristic of bulk-type V_2O_3 (Ref. 20) at coverages > 2.5 MLE.

Both STM and photoemission data indicate that the vanadium oxide overlayer on Rh(111) evolves in different oxide phases during the growth process: initially, a higher oxidized phase is formed in the first monolayer, which transforms into a more complex phase, with several coexisting oxide structures, between 1 and 2 ML. The oxide layer converges to a bulk-type V_2O_3 phase for thicker films (>2 MLE).

B. Oxide structures for $\Theta < 0.6$ MLE

The STM image of Fig. 4(a) shows part of a large vanadium oxide island for $\Theta \sim 0.25$ MLE, as prepared by reactive evaporation in 2×10^{-7} mbar O_2 at 400 °C substrate

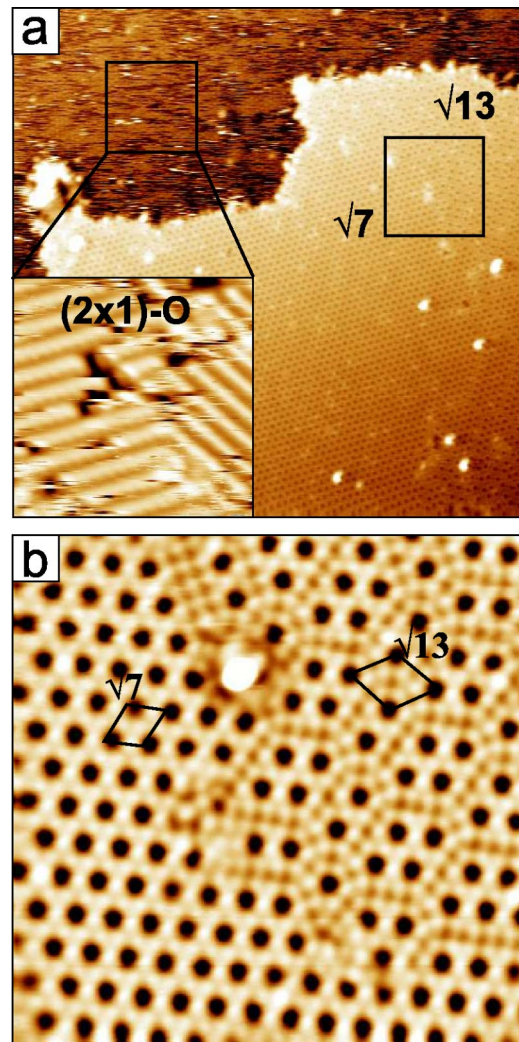
FIG. 4. (a) STM image (500×500 Å^2, $U = 1.5$ V, $I = 0.2$ nA) showing a 2D island together with the O-covered Rh substrate surface. The inset (50×50 Å^2, $U = 0.4$ V, $I = 0.1$ nA) shows the O-(2×1) structure. (b) Magnified view of the area marked by the frame on the right in image (a): 100×100 Å^2, $U = 0.69$ V, $I = 0.1$ nA. Unit cells of the $(\sqrt{7} \times \sqrt{7})R19.1°$ and $(\sqrt{13} \times \sqrt{13})R13.8°$ structures are indicated.

temperature. The oxide island is well ordered and displays a hexagonal lattice structure. The apparent height of the island is 1.6 ± 0.2 Å, as referred to the bare rhodium surface. This height is slightly dependent on the tunneling conditions and varies between 1.4 Å(tunneling bias of $+2$ V) and 1.7 Å (tunneling bias of $+0.5$ V). Principally, this measured height suggests a single vanadium oxide layer. On the bare Rh(111) surface areas in between the oxide islands the (2×1)-O structure of chemisorbed oxygen[21] is visible, as shown by the inset of Fig. 4(a): the bright rows correspond to the Rh and the dark lines to the oxygen atoms. Closer inspection of Fig. 4(a) reveals that the oxide island is actually composed of two different structures, which are separated by a phase boundary running from top to bottom in the right-hand part of the image. A magnified view of this phase boundary region, marked by the frame in the image (a), is presented in Fig. 4(b). The phase on the left-hand side of the image cor-
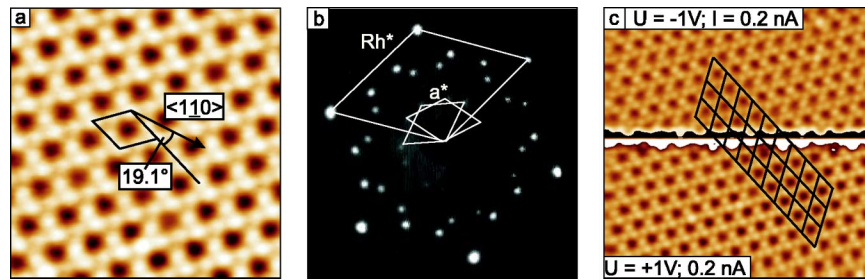
FIG. 5. (a) High-resolution STM image (50×50 Å^2, $U = 0.75$ V, $I = 0.2$ nA) of the $(\sqrt{7} \times \sqrt{7})R19.1°$ oxide phase. (b) LEED pattern ($E = 55$ eV) of the $(\sqrt{7} \times \sqrt{7})R19.1°$ structure. The reciprocal unit cells of the Rh substrate and the oxide overlayer are indicated and labeled Rh* and a*, respectively, on the LEED pattern. (c) 100×100 Å^2 scan of the $\sqrt{7}$ structure with a tunneling voltage polarity change in the middle of the image from $U = 1$ V to $U = -1$ V.

responds to a $(\sqrt{7} \times \sqrt{7})R19.1°$ with the respective unit cell indicated. The right-hand side of the image consists of a mixture of the $(\sqrt{7} \times \sqrt{7})R19.1°$ phase and locally ordered units with a $(\sqrt{13} \times \sqrt{13})R13.8°$ symmetry. For shortness reasons we will refer to these two structures in the following as $\sqrt{7}$ and $\sqrt{13}$. The coexistence of the two phases in the same island and the smooth boundary separating them suggest that the $\sqrt{7}$ and $\sqrt{13}$ structures are energetically closely related. We found, however, two different kinetic routes to prepare each of these structures as a unique phase at the surface. A well-ordered $\sqrt{7}$ structure can be obtained as a single phase by reactive evaporation at 250 °C substrate temperature in 5×10^{-8} mbar O$_2$ with an evaporation rate of ~ 0.25 MLE/min, whereas likewise a single $\sqrt{13}$ structure is prepared by evaporating first V metal with the substrate at room temperature and postoxidation at 400 °C in 2×10^{-7} mbar O$_2$.

The $\sqrt{7}$ structure is analyzed in Fig. 5. The high-resolution STM image of Fig. 5(a) shows the structural details at the atomic scale, with a hexagonal lattice that consists of three bright protrusions per unit cell. The sharp LEED pattern [Fig. 5(b)] confirms the high structural order and the unit-cell dimensions. In order to identify the nature of the observed protrusions in the STM images, it is necessary to investigate whether geometry or electronic effects dominate the imaging process in the STM. In Fig. 5(c) the polarity of the sample bias voltage has been switched during the recording of the STM image, from positive (bottom part) to negative (top part) in the middle of the STM image. As it is seen and confirmed by the grid of lines in the figure the protrusions all line up, indicating that the maxima in the STM image can be taken as the position of atomic species. For V oxides on Pd(111) density-functional-theory (DFT) based simulations of STM images have established that the V atoms are imaged under the same experimental conditions as employed here.[3] The bright maxima in the STM images in Fig. 5 were therefore initially associated with the V atoms of the $(\sqrt{7} \times \sqrt{7})R19.1°$ structure. We will see below that this assignment is however not quite correct.

The nature of the $(\sqrt{13} \times \sqrt{13})R13.8°$ structure is investigated in Fig. 6. The STM image of Fig. 6(a) reveals a hexagonal unit mesh containing six protrusions. Figure 6(b) shows the LEED pattern with two $\sqrt{13}$ unit cells rotated by $\sim 13.8°$ with respect to the $[1\bar{1}0]$ direction, as also indicated

on the STM image. As for the $\sqrt{7}$ structure, STM images obtained with positive and negative bias show the same structural details and for the reasons mentioned above it was concluded that the V atoms are imaged also here. In Fig. 6(c) the V $2p_{3/2}$ core-level spectrum for the $\sqrt{13}$ structure, prepared as a single phase, is presented. The spectrum displays a broad peak, which requires two components in the decomposition analysis. The major spectral component is obtained at a BE of 515.2 eV, while a second component is located at 516.1 eV. The binding energy of 515.2 eV would be formally compatible with a V$_2$O$_3$ stoichiometry.[19] However, it has been found previously[22] that the core-level binding energies of metal atoms in ultrathin oxide overlayers cannot be taken *prima facie* as a measure of the oxidation state of the metal atoms as a result of the final-state effects introduced by the adjacent metal substrate. Therefore, the binding energy of 515.2 eV is not necessary a safe indication of the 3^+ oxidation state, but may also be compatible with a higher oxidation state. The origin of the minority V $2p_{3/2}$ component at 516.1 eV is unclear at present; perhaps it is associated with effects at the island boundaries. Interestingly, the XPS spectrum of the $\sqrt{7}$ structure (not shown) is virtually identical with the spectrum of the $\sqrt{13}$ structure, with two peak components derived from the curve-fitting analysis at 515.2 and 516.1 eV. Also valence-band spectra and HREELS data of the two oxide structures do not show any significant differences. Figure 6(d) shows a HREELS spectrum of the $\sqrt{13}$ ($\sqrt{7}$) structure and reveals two sharp phonon modes at 65 meV and 130 meV loss energy. While the loss peak at 65 meV is typical of bridging oxygen atoms in V-O-V configurations,[5] the loss at 130 meV has to be associated with the stretching vibrations of V=O groups,[5] i.e., the $\sqrt{13}$ ($\sqrt{7}$) structures must contain vanadyl groups as structural units.

The determination of a reasonable structural model for the $\sqrt{7}$ ($\sqrt{13}$) phases was based, as before, on extensive *ab initio* modeling making use of finite temperature molecular dynamics, when appropriate. The stringent requirements for reasonable candidates are (i) that they should remain structurally intact at finite temperature molecular dynamics up to 1200 K, and (ii) that they should be thermodynamically stable in the VxOy/Rh(111) surface phase diagram constructed according to the prescription of Ref. 16. To this end the energies of all stable oxide phases on Pd(111) were reevaluated
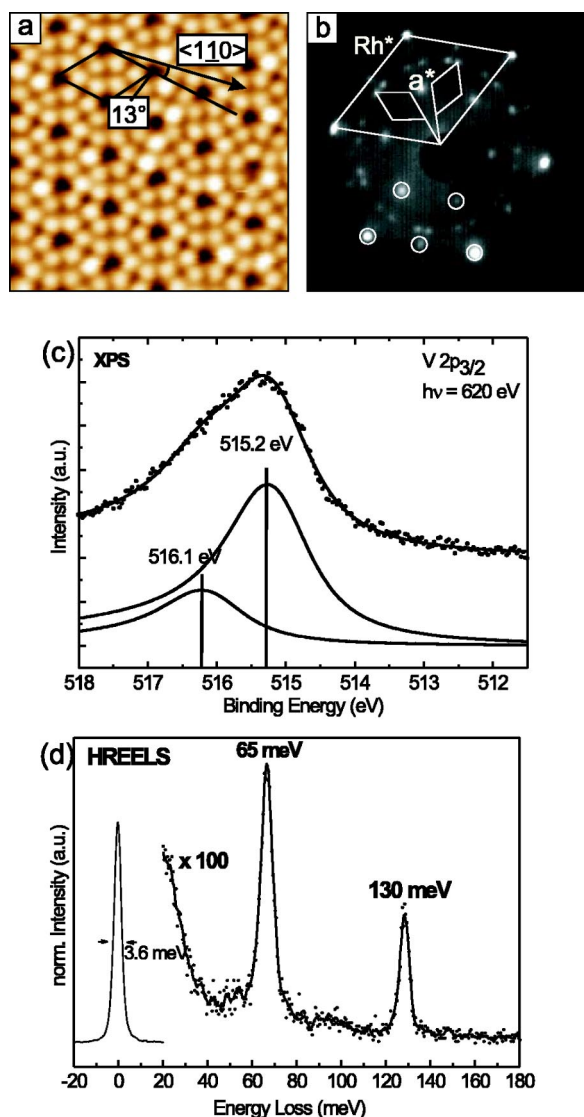
FIG. 6. (a) Atomically resolved STM image of the ($\sqrt{13} \times \sqrt{13})R13.8°$ structure (50×50 Å^2, $U = -1$ V, $I = 0.4$ nA). (b) LEED pattern of the ($\sqrt{13} \times \sqrt{13})R13.8°$ oxide phase. Reciprocal unit cells of substrate (Rh*) and oxide overlayer (a*) are indicated by thin white lines together with spots due to the (2×1)-O covered surface areas (circles), which form a (2×2) diffraction pattern. (c) High-resolution XPS spectrum of 0.25 MLE VOx/Rh(111) for the ($\sqrt{13} \times \sqrt{13})R13.8°$ oxide phase. A Shirley background has been subtracted. (d) HREELS phonon spectrum of the ($\sqrt{13} \times \sqrt{13})R13.8°$ structure recorded in specular scattering geometry.
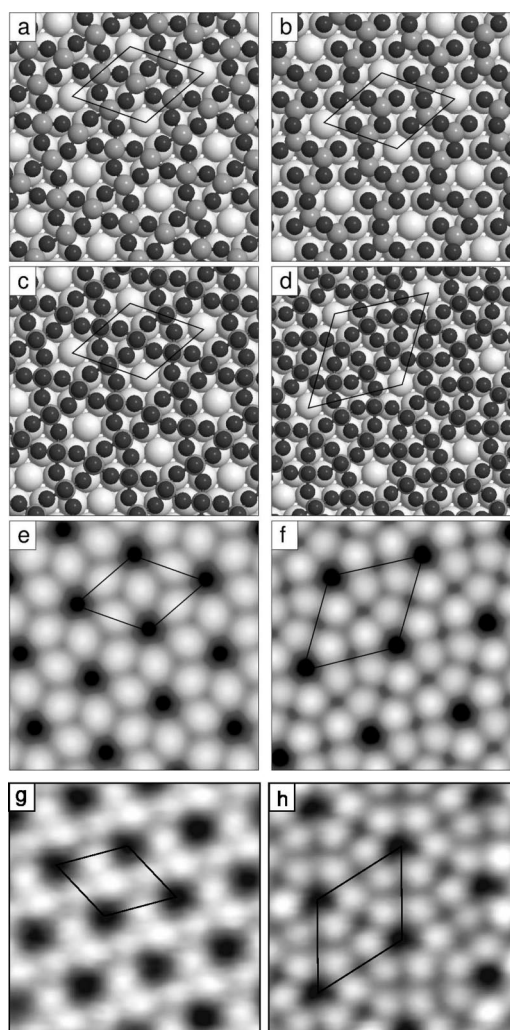

FIG. 7. Structure models for the $\sqrt{7}$ (a–c) and $\sqrt{13}$ (d) oxide phases. Dark gray spheres represent oxygen, medium gray spheres vanadium, and light gray spheres rhodium atoms. The respective unit cells are indicated in the models. Simulated STM images of the $\sqrt{7}$ and $\sqrt{13}$ structures are shown in (e) and (f), respectively. Corresponding experimental STM images (25×25 Å^2, $U = 1$ V, $I = 0.2$ nA) are displayed in (g) and (h), respectively.

on Rh(111). It is emphasized that criterion (ii) is not particularly easy to meet, since stable structures on Pd(111) are generally found to have even larger adsorption energies on Rh(111), because the bonding of ultrathin oxide layers to the substrate is even stronger on Rh(111) than on Pd(111).

Screening of possible structural models for the $\sqrt{7}$ phase started from an educated guess suggested by the STM images and the observation that bright spots are usually associated with V atoms.[3] The corresponding structural model is shown in Fig. 7(a). It is characterized by three V atoms in the unit cell positioned in the bridge sites, with four oxygen neighbors each. For symmetry reasons the O atoms were located roughly above Rh atoms in the surface layer. The simulated STM image (not shown) upon first inspection exhibits rough agreement with experiment, but the model has several shortcomings that rule it out as a reasonable candidate for the experimentally observed structure. First, the structure was not sufficiently stable to show up in the VxOy/Rh(111) surface phase diagram. This in itself is not an entirely sufficient argument, since it is well possible that the structure is stabilized by kinetics instead of thermodynamics. More importantly, however, the structure was found to disintegrate during a finite temperature molecular dynamics (MD) at 1500 K resulting in a lower-energy structure which lacks the proper symmetry. The final structure of the finite temperature MD, shown in Fig. 7(b), is remarkable in itself, as it contains structural motives of the well studied surface-V$_2$O$_3$ structure found on Pd(111):[3] the vanadium at-

oms are located in the threefold hollow sites and are coordinated to three oxygen atoms each. The oxygen atoms are either bridge bonded between two vanadium atoms, or linked to a single vanadium atom—the only building block that was not observed on Pd(111). As the lower symmetry already suggests, the STM simulation exhibits no similarity with the experimental topographs. Several attempts with structures containing less oxygen such as V_3O_5 were also unsatisfactory in yielding a stable structure with the proper symmetry. The only point worthwhile noting is that these simulations lead to similar structural units as observed in Fig. 7(b), which is a strong indication that such structural motives are relevant if the ratio between oxygen and vanadium is $\approx 2:1$. But such structures are not consistent with the experimentally observed STM images.

For the final structure determination, the crucial experimental information was supplied by the HREELS measurements that became available during the modeling. They exhibit a clear signal at 130 meV, which suggests that the surface oxide contains V=O groups. It was tempting to add one additional oxygen atom on top of each vanadium atom, thus forming a double-bonded vanadyl oxygen species [Fig. 7(c)]. As before the structure was subjected to an extensive finite temperature molecular dynamics at 1000 K and remained intact throughout the simulation. Only at higher temperatures, the registry with the substrate changed temporarily but reverted to the initial one after cooling to lower temperatures. The structure is also found to be thermodynamically stable in the surface phase diagram for V_xO_y/Rh(111) at sufficiently oxidizing conditions (i.e., at those conditions at which the Rh (2×1)-O structure is stable as well). The final optimized structure is shown in Fig. 7(c). The oxygen atoms are found to be roughly in on-top positions with a vertical Rh-O distance of 2.05 Å. The vanadium atoms are located 0.56 Å above the oxygen layer in bridge position of the substrate. The large V-Rh distance suggests that their bonding to the substrate is only through the interfacial oxygen atoms. Roughly 1.6 Å above each vanadium atom and 4.2 Å above the substrate, one double-bonded oxygen atom is located. The structure is therefore oxygen terminated on both, metal-oxide and oxide-vacuum, interfaces and consists of pyramidally coordinated V atoms. This is similar as in the V_2O_5 bulk structure, which consists of pyramidally edge- and corner-shared coordination polyhedra, as well. A similar but tetrahedral V-O coordination has been found recently for a (4×4)-V_5O_{14} phase on Pd(111) on the basis of DFT calculations.[6,23] Similar as for that phase, the formal oxidation state of the V atoms is not in conflict with the maximum $5+$ oxidation state, because the six O atoms are shared with the substrate. In fact, we calculate an adsorption energy of 8.6 eV per oxide unit cell or 1.4 eV per O-Rh bond for bringing the surface oxide from the vacuum to the substrate, which indicates a significantly larger substrate-oxide interaction than for surface oxides on Pd(111).[16,23]

The STM simulation of the $\sqrt{7}$ oxide phase is shown in Fig. 7(e). The density at which the isosurfaces were calculated was chosen such that the isosurfaces were evaluated at a distance of 4.2 Å from the topmost surface atom on the clean Rh(111) substrate. As expected the vanadyl groups are imaged as bright blobs and the simulation is found to be almost independent of bias, which agrees with the experimental observation. The bright spots have a height of 2 Å with respect to the clean substrate in excellent agreement with experiment (and much smaller than one would expect on simple geometric grounds). Nevertheless, the observed corrugation is a result of the large geometrical corrugation, as already suggested by the bias-independent experimental constant current topographs.

A further confirmation of the structure comes from the simulated HREELS spectrum. Only two vibrational modes at 137 meV and 65 meV are found to have a large dipole intensity. The one at 137 meV originates from the V=O bond stretch and is found at a somewhat too high frequency compared to the experiment (as in previous studies[6]). The second vibrational mode—which is in excellent agreement with experiment—corresponds to vibrations of the interfacial oxygen atoms normal to the substrate. The spectroscopic similarity of the $\sqrt{7}$ with the $\sqrt{13}$ structure suggests similar or identical building units for the two structures. Indeed, the $\sqrt{13}$ structure can be constructed readily by using the pyramidal coordination polyhedra and the known arrangement of V ions within the unit cell, as derived from the STM images. Figure 7(d) shows the final relaxed model of the $\sqrt{13}$ structure consisting of a V_6O_{18} unit cell and Fig. 7(f) the corresponding STM simulation. The simulated STM images of both $\sqrt{7}$ and $\sqrt{13}$ structures agree almost perfectly with the experimental STM images displayed in Figs. 7(g) and 7(h), thus supporting the DFT models.

The V atom density of the $\sqrt{7}$ structure, with $\Theta = 0.43$ MLE for a full monolayer coverage, is slightly lower than that of the $\sqrt{13}$ structure ($\Theta = 0.46$ MLE). Energetically the $\sqrt{7}$ structure is preferred over the $\sqrt{13}$ structure, when the formation energy E_{form} is calculated per VO_3 unit, as expected for a model with lower packing density. But the surface energy $E_{surface}$, which is the decisive quantity for the structural stability, is lower for the $\sqrt{13}$ structure, since the reduced formation energy is more than compensated by the increased coverage

$$\Delta E_{surface} = \Theta E_{form}.$$

This suggests that the thermodynamically stable phase is in fact the $\sqrt{13}$ phase, whereas the $\sqrt{7}$ phase is only kinetically trapped, e.g., upon reactive evaporation.

Experimentally, the completion of the first oxide layer is observed at around 0.5–0.6 MLE, which is somewhat larger than the theoretical values derived from the structure models. Lateral inhomogeneities on the surface could contribute to this discrepancy, such as the presence of oxide islands with a higher V atom density. Annealing the $\sqrt{7}$ and $\sqrt{13}$ V-oxide layers at elevated temperatures in UHV or in H_2 atmosphere results in a complex sequence of reduced oxide phases. This will be treated in a forthcoming paper.[24] Here we mention that the $\sqrt{7}$ and $\sqrt{13}$ structures are stable up to ~ 600 °C, if the residual H_2 partial pressure in the UHV system is kept below 10^{-11} mbar.
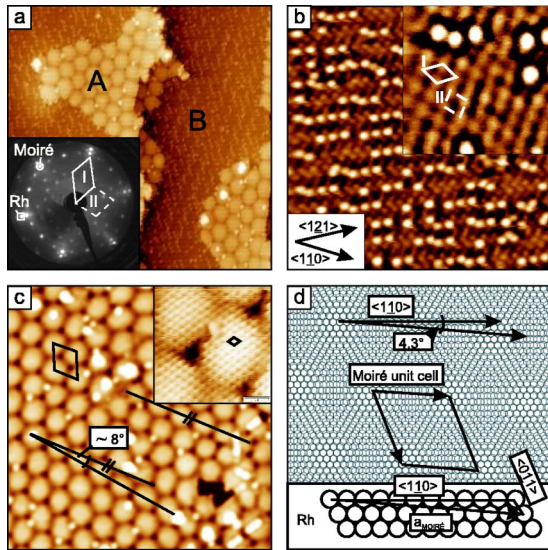
FIG. 8. (a) 500×500 Å^2 STM image of 0.7 MLE VOx/Rh(111) prepared at 400 °C substrate temperature in 2×10^{-7} mbar O$_2$ ($U = 2.0$ V, $I = 0.1$ nA). Areas labeled A and B show the Moiré and the ''oblique'' oxide structures, respectively. The inset displays the LEED pattern of this surface. (b) High-resolution STM image (150×150 Å^2, $U = 2$ V, $I = 0.1$ nA) of areas labeled B in image (a). The inset shows a 50×50 Å^2 scan ($U = 1.5$ V, $I = 0.1$ nA), with two possible unit cells indicated. (c) STM image of areas labeled A in (a) showing the Moiré pattern (300×300 Å^2, $U = 1.75$ V, $I = 0.05$ nA). The inset displays an atomically resolved STM image revealing the internal hexagonal unit-cell structure of the Moiré pattern (50×50 Å^2, $U = 25$ mV, $I = 1.5$ nA). (d) Rigid sphere model illustrating the formation of the Moiré pattern (see text).

C. The transition regime $0.6 < \Theta < 1.2$ MLE

As already mentioned in Sec. III A, the vanadium oxide layer undergoes a complex phase transformation in the coverage range 0.6–1.2 MLE, i.e., after the first oxide layer has been completed. Although the observed oxide structures are identical for the two employed deposition temperatures (substrate at ~ 250 °C or ~ 400 °C), the overall morphology of the oxide overlayer is significantly different with better ordering achieved at ~ 400 °C. Therefore, the latter situation will be considered in detail and the differences to the ~ 250 °C case will only shortly be mentioned.

Figure 8(a) shows a large-scale STM image for an oxide coverage of 0.7 MLE, where two phases (marked A and B) can be distinguished on the surface. The areas marked A cover $\sim 30\%$ of the surface (at this particular coverage) and show an ordered array of hexagons with a periodicity of 30.5 ± 1.0 Å and a corrugation of about 0.6 Å. The structure is presented in more detail in Fig. 8(c). The inset of Fig. 8(c) shows that the hexagons exhibit an internal structure (the unit cell is indicated on the image) with a lattice constant of 2.9 ± 0.2 Å and a corrugation amplitude of ~ 0.1 Å. This suggests a Moiré origin for the large-scale modulations. The lattice parameter is also confirmed by the LEED pattern [inset of Fig. 8(a)], yielding a value of 2.91 ± 0.05 Å. In the STM image of Fig. 8(c) two lines running along different rows of the Moiré lattice are drawn, which enclose an angle

of $\sim 8° \pm 1°$. The origin of this rotational angle can be understood on simple geometrical grounds. In a rigid sphere model [Fig. 8(d)] a rotational mismatch of $\alpha = 0.4°$ between the VOx layer (lattice constant of 2.91 Å) and the Rh(111) substrate leads to coincidence sites on the rhodium surface: 11 Rh lattice spacings along the $[1\bar{1}0]$ direction and one Rh lattice spacing along the $[0\bar{1}1]$ direction. This is illustrated at the bottom of Fig. 8(d). The resulting coincidence overlayer structure has a large unit cell of 31.02 Å, which agrees well with the experimentally observed Moiré periodicity, and is rotated by 4.3° with respect to the (1×1) unit cell of the Rh(111) surface. Thus, two domains of the oxide overlayer rotated by $\pm 0.4°$ with respect to the rhodium $[1\bar{1}0]$ direction would generate two domains of the Moiré structure, the latter enclosing an angle of $2 \times 4.2° = 8.6°$, thus corroborating the experimental result. Occasionally, smaller (between 4° and 5°) rotational angles between the Moiré rows are observed in the STM images, which is indicative of a weak coupling between the oxide overlayer and the metal substrate.

In previous work DFT calculations[16] have established that a VO$_2$-type phase with a hexagonal structure and a relaxed lattice parameter of $a = 2.87$ Å (i.e., very close to the experimentally observed value of 2.91 Å of the Moiré phase) may become stable in the form of a thin unsupported layer. This model structure has been obtained by cleaving a VO bulk crystal structure along two (111) planes leading to a hexagonal layer of V atoms sandwiched between two hexagonal oxygen layers.[16] Such a hexagonal (hex) VO$_2$-type phase has been experimentally identified in STM images to grow as a pseudomorphic layer on Pd(111) in the coverage regime $0.8 < \Theta < 1.2$ MLE.[4] Since the hex-VO$_2$ structure is stable in this layer form without a metal support, it might be also present on other substrate materials. These similarities suggest that the Moiré phase on Rh(111) is analogous to the hex-VO$_2$ structure observed on Pd(111). The appearance of the hex-VO$_2$ phase as a Moiré pattern on Rh(111), but not on Pd(111), is due to the small difference of 2% between the in-plane lattice constants of the Rh and Pd(111) surfaces.

Figure 8(b) shows a STM image with higher resolution from the B-type areas of Fig. 8(a). Two kinds of protrusions are seen on this structure, which are imaged with different apparent heights. The maxima appearing with lower contrast in the STM images form an oblique unit cell, which can be chosen in two different ways with similar unit-cell areas [see inset of Fig. 8(b)]. This oxide structure will be designated as ''oblique phase'' in the following. The matrix notations for the oblique unit cells are $I = \begin{pmatrix} 1.16 & 1.16 \\ -1.72 & 2.20 \end{pmatrix}$, $II = \begin{pmatrix} 1.16 & 1.16 \\ -1.10 & 2.90 \end{pmatrix}$, which indicate incommensurable structures. The protrusions imaged with higher contrast do not form an extended regular lattice. They appear in on-top positions above the oblique lattice maxima (relative apparent height 0.7 Å) and tend to align along the $[1\bar{2}1]$ substrate directions with a separation of 5.4 Å.

The HREELS spectrum of a 0.8 MLE vanadium oxide film is shown in Fig. 9: it contains an intense phonon loss peak at 128 meV, which is characteristic for vanadyl species.[5] Thus the bright irregular protrusions in Fig. 8(b) may be identified
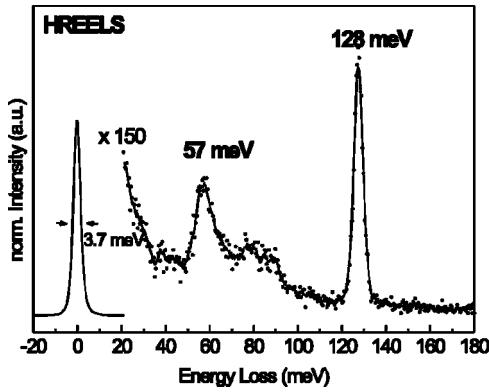
FIG. 9. HREELS phonon spectrum of a 0.8 MLE vanadium oxide film on Rh(111) prepared at 400 °C.

FIG. 10. (a) STM image of a 1.0 MLE vanadium oxide film (200×200 Å^2, $U = 1.8$ V, $I = 0.1$ nA). Four different oxide phases can be recognized in the image as indicated. (b) Filtered STM image revealing that the b-V$_2$O$_3$ phase nucleates on top of the Moiré pattern (215×215 Å^2, $U = 1$ V, $I = 0.1$ nA). (c) Atomically resolved STM image of the "wagon-wheel" phase. (100×100 Å^2, $U = 0.1$ V, $I = 0.1$ nA). One "wagon-wheel" unit is indicated on the image. The inset shows the LEED pattern of this surface. (d) Autocorrelation image of the STM image (c).

as vanadyl oxygen atoms. A phase with a "zigzag" structure and similar features in STM and HREELS as in the oblique structure here was also observed for the VOx/Pd(111) system,[25] where it has been rationalized in terms of a V$_6$O$_{14}$ phase by DFT calculations.[6]

The complex LEED pattern [inset of Fig. 8(a)] may now be explained as a superposition of diffraction reflections originating from the A- and B-type oxide areas. Next to the Rh (1×1) spots (indicated by a square) diffraction reflexes due to the Moiré-VO$_2$ phase (circle) are visible. The latter reflexes can be described in terms of multiple-scattering processes between the rhodium substrate and the oxide overlayer and/or diffraction from the large superstructure unit cells of the buckled overlayer. Both descriptions lead to the same LEED pattern. Additional LEED spots originate from the oblique oxide phase between the Moiré islands. Both oblique unit cells are indicated on the LEED picture, and both generate the experimentally observed pattern, taking into account all valid symmetry operations of the substrate.

For oxide coverages in the range of 1 MLE the Moiré phase decreases again in area [see, e.g., Fig. 2(e)] and the nucleation of additional oxide layers commences on top of the Moiré islands. This becomes evident from the STM image in Fig. 10(a), which shows a Moiré island covered by oxide layers with (2×2) and ($\sqrt{3} \times \sqrt{3}$)$R30°$ periodicities with respect to the Rh(111) lattice. This resembles again the growth behavior observed for VOx/Pd(111), where (2×2) and ($\sqrt{3} \times \sqrt{3}$)$R30°$ phases also form in this coverage regime.[5] The (2×2) overlayer has been modelled in previous DFT calculations as a V$_2$O$_3$-type V-O double layer on top of the hexagonal VO$_2$ phase, and was found to energetically stabilize the hex-VO$_2$ phase upon further oxide growth.[4] The resulting structure has an overall stoichiometry of V$_6$O$_{11}$ and may be regarded as a precursor of the bulk-type V$_2$O$_3$ (b-V$_2$O$_3$) phase, which develops at higher coverages. The latter exhibits a ($\sqrt{3} \times \sqrt{3}$)$R30°$ structure in the STM images. A hex-VO$_2$ island fully covered by the b-V$_2$O$_3$ phase is shown in the STM image in Fig. 10(b), where the atomic corrugation of the ($\sqrt{3} \times \sqrt{3}$)$R30°$ structure is superimposed on the large-scale modulation of the Moiré pattern. The b-V$_2$O$_3$ phase grows with the (0001) plane of the corundum structure parallel to the Rh(111) surface, with an in-
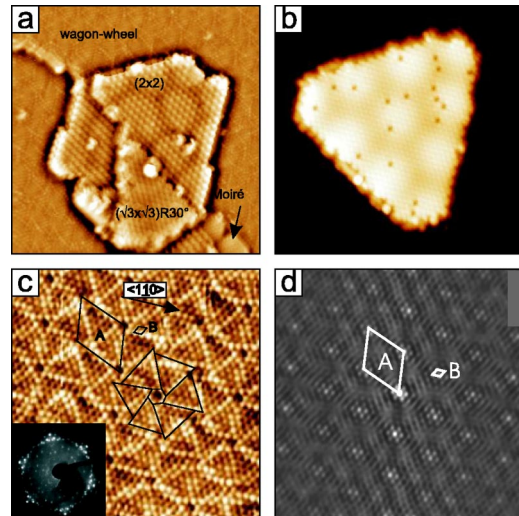
plane lattice constant of 4.9 ± 0.1 Å. The misfit between the b-V$_2$O$_3$ lattice vectors and the diagonal of the hex-VO$_2$ unit cell is 2.8%, which is much less than the 5.1% between the b-V$_2$O$_3$ and Rh(111) lattices. The hex-VO$_2$ structure thus creates a graded interface to accommodate the lattice mismatch between Rh(111) and b-V$_2$O$_3$. This is similar to the situation encountered for V oxides on Pd(111), where a hex-VO$_2$ layer also mediates the growth of the bulk-type V$_2$O$_3$ phase.[5]

High-resolution STM images reveal that at this stage of the oxide overlayer growth the oblique structure in between the b-V$_2$O$_3$ islands has been replaced by another oxide phase, which is shown in Fig. 10(c). The latter exhibits the so-called wagon-wheel-like structure, which is similar to those reported previously for V-oxide films on Pd(111),[2] Pd on TiO$_2$(110),[26] and for a Cr/Pt(111) alloy superstructure.[27] The wagon-wheel pattern is indicated by thin lines on the STM image of Fig. 10(c): the center is imaged dark and surrounded by six bright features forming a hexagon. From each maximum of this hexagon more or less straight rows of brighter protrusions run outwards. These rows are almost parallel to the $[1\bar{1}0]$ directions of the substrate. Since it is difficult to define a unit cell due to the imperfect ordering, autocorrelation of the STM images has been used to assess the unit-cell dimensions. First, a large hexagonal unit cell [marked A in Fig. 10(c)] is recognizable and its lateral dimension is measured to 18.9 ± 0.2 Å. The rotational angle between the main $[1\bar{1}0]$ substrate directions and the unit cell is $\alpha = (21 \pm 1)°$, which corresponds to a $(7 \times 7)R21.8°$ structure. The autocorrelation image [Fig. 10(d)] reveals in addition that locally the maxima in the STM image form a

hexagonal lattice (the unit cell marked B in the STM image). The average interatomic distance is about 3.1 ± 0.2 Å. As will be shown in more detail in a forthcoming paper[24] the complex wagon-wheel structure is in fact a Moiré pattern resulting from the superposition of the hexagonal lattices of the oxide film (with a lattice spacing of 3.1 Å) and the Rh(111) substrate.

The wagon-wheel structure can be prepared at submonolayer coverages as a single phase by evaporating 0.5 ML V metal in UHV onto an oxygen predosed Rh(111)-(2×1)-O surface at room temperature (with an oxygen saturation coverage of 0.5 ML). This provides a direct estimate for the stoichiometry of the wagon-wheel phase, yielding a V:O ratio of 1:1, or a VO stoichiometry.[24] A V-O bilayer with a hexagonal structure can be modeled by cleaving a bulk VO crystal parallel to the (111) planes. The experimentally determined lattice spacing of the wagon-wheel structure (3.1 Å) deviates slightly from the lattice constant of the unreconstructed VO (111) surface (2.89 Å). Since the latter surface is polar and considered to be unstable due to its nonvanishing surface dipole,[28] the observed lateral expansion of the vanadium-oxygen interatomic distance reflects presumably a reduction of the interlayer spacing, and thus a decrease of the surface dipole. In addition, the metal substrate can compensate the dipole in the oxide layer by an image dipole and this can also stabilize the VO bilayer. A similar mechanism has also been invoked to explain the initial growth of ultrathin FeO(111) layers on Pt(111).[29,30] Since no CO, CO_2, or H_2O could be adsorbed on the wagon-wheel VO surface at room temperature, it is concluded that the VO bilayer is oxygen terminated at the oxide-vacuum interface.

The XPS spectra of Fig. 3(a) substantiate the stoichiometric assignments of the various oxide structures forming in the transition regime from monolayer to three-dimensional (3D) growth. For oxide coverages of ~ 1 MLE the surface is predominantly covered by the wagon-wheel wetting layer and some hex-VO_2 (Moiré) islands, capped by (2×2) and/or $(\sqrt{3} \times \sqrt{3})R30°$ layers [see Figs. 2(e) and 10(a)]. Correspondingly, the V $2p$ core-level spectra [Fig. 3(a)] contain a major component with a binding energy of ~ 513.8 eV, indicating a formal V oxidation state of 2^+, and this supports the assignment of the wagon-wheel layer as a VO-like phase. The sharp peak at the Fermi level [valence-band spectra for 1.0 and 1.2 MLE in Fig. 3(b)], due to the V $3d$ emission, is also in line with the VO stoichiometry, since band-structure calculations for stoichiometric VO (Ref. 31) have shown that the Fermi energy lies within the d band. The minor V $2p$ core-level component at ~ 515.8 eV [Fig. 3(a)] corresponds to a formal V oxidation state of 3^+, which corroborates the identification of the (2×2) and $(\sqrt{3} \times \sqrt{3})R30°$ layers as V_2O_3-type species. Increasing the oxide coverage above 1 MLE results in the progressive growth of the b-V_2O_3 3D islands, which is reflected in the gradual shift of the V $2p$ spectral weight to higher binding energies. This trend continues until the b-V_2O_3 phase is fully established.

D. Thick oxide layers $\Theta > 2$ MLE

For coverages exceeding 2 MLE only the b-V_2O_3 phase is stable under the present experimental conditions. Figure
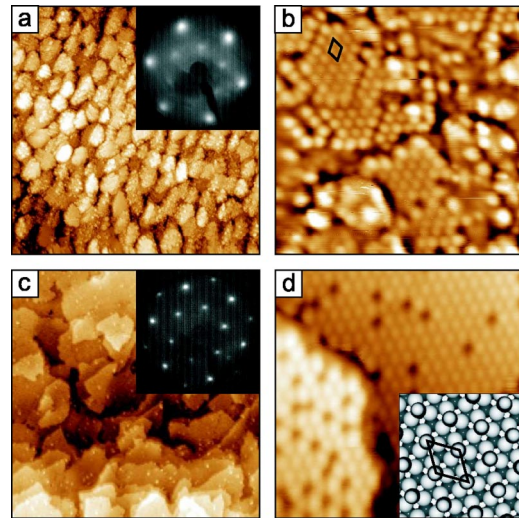

FIG. 11. (a,b) STM images of thick ($\Theta = 10$ MLE) vanadium oxide layers prepared at 250 °C in 2×10^{-7} mbar O_2. Image (a) is a 1000×1000 Å^2 scan ($U = 1.25$ V, $I = 0.25$ nA) and image (b) is a 100×100 Å^2 scan ($U = 1.25$ V, $I = 0.25$ nA), showing elements of the hexagonal bulk V_2O_3 structure. (c,d) STM topographs of a 7 MLE thick vanadium oxide film evaporated at 400 °C substrate temperature. Image (c) is a 1000×1000 Å^2 scan ($U = 1.75$ V, $I = 0.15$ nA) and (d) shows a 100×100 Å^2 scan ($U = 2$ V, $I = 0.1$ nA). The insets in (a) and (c) display the LEED patterns for the corresponding surfaces. A model for the vanadyl-terminated surface is shown in the inset of (d): light gray spheres represent oxygen atoms and dark gray spheres represent vanadium atoms. The vanadyl groups form the corners of the unit cell.

11(a) displays a STM image of a 10 MLE thick vanadium oxide film deposited at 250 °C. At this substrate temperature the oxide grows in the form of randomly shaped grains of three-dimensional crystallites with lateral dimensions ranging from 50 to 150 Å. The atomically resolved STM image in Fig. 11(b) reveals that the degree of structural order of the b-V_2O_3 surface is poor, as evident from the large number of step edges, missing protrusions, and grain boundaries. This is also corroborated by the diffuse $(\sqrt{3} \times \sqrt{3})R30°$ LEED pattern, taken from this surface [inset of Fig. 11(a)].

Preparing thick oxide films at a substrate temperature of 400 °C [10 MLE in Figs. 11(c) and 11(d)] results in the formation of much larger terraces and better ordering. This is confirmed by the sharper LEED pattern displayed in the inset of Fig. 11(c). The atomically resolved STM image [Fig. 11(d)] reveals the hexagonal unit cell of the (0001) plane of b-V_2O_3. As already established in our previous work[5] the V_2O_3(0001) surface is terminated by V=O (vanadyl) species yielding a stacking sequence: —O_3—V_2—O_3—V=O [see the model in the inset of Fig. 11(d)]. This model is supported by the HREELS spectrum shown in Fig. 12(a), which shows a phonon loss peak at 129 meV, which is characteristic for the vanadyl groups.[32] The other phonon peaks at 47, 79, and 92 meV are typical for the bulk-V_2O_3 structure.[33] The XPS spectrum, taken in the V $2p$ and O $1s$ core-level region [Fig. 12(b)] confirms the V_2O_3 stoichiometry, since the main spectral components of the V $2p_{3/2}$ and O $1s$ peaks are located at binding energies of 515.6 eV (la-
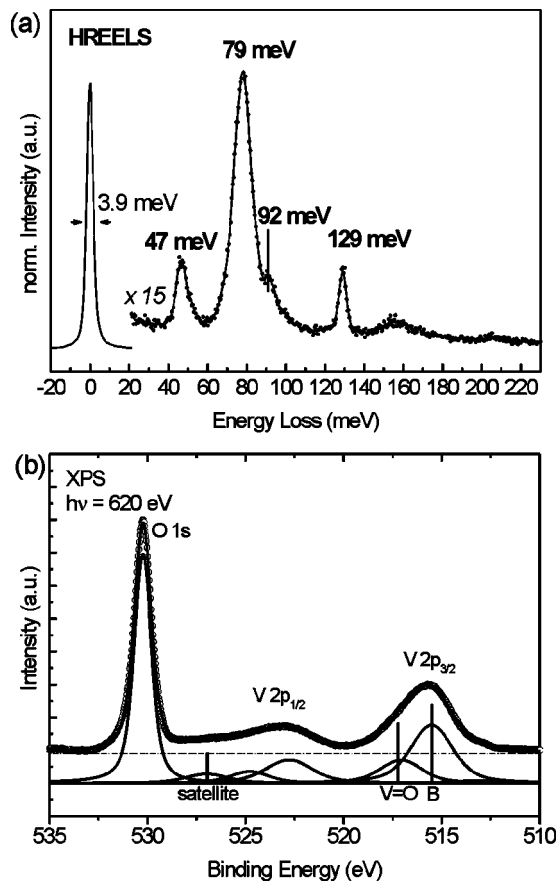
FIG. 12. (a) HREELS spectrum of the vanadyl-terminated V_2O_3 (0001) surface prepared at 400 °C substrate temperature. (b) XPS spectrum of the O 1s and V 2p core levels of 20 MLE V oxide grown at 400 °C substrate temperature. Two components are identified in the V 2p core levels due to emission from bulk vanadium atoms (marked B) and vanadium atoms at the surface (marked V=O). A charge transfer satellite is visible at ~527 eV binding energy.

beled B) and 530.1 eV, respectively; these data agree well with the corresponding literature values for corundum V_2O_3 single crystals.[19] A second component at the higher binding energy of 517.5 eV was necessary to fit the spectrum adequately, as also reported by Dupuis et al.,[34] who assigned this component to the V atoms in the terminating V=O groups. A similar sequence of core-level components, as for the V 2$p_{3/2}$ peak, has been used for the decomposition analysis of the V 2$p_{1/2}$ peak, with the corresponding intensities reduced by a factor of 2 and the peak positions shifted to higher energies by the value of the doublet splitting (~7.3 eV). In addition, a component at ~526.9 had to be taken into account in the decomposition analysis of the V 2$p_{1/2}$ peak, which is associated with a charge transfer satellite due to the interaction of the V 2p core hole with the valence-band electrons.[20]

IV. DISCUSSION

Figure 13 summarizes the sequence of structures, which have been observed during the growth of V-oxide thin films

FIG. 13. Sequence of oxide structures forming during the growth of V-oxide films on Rh(111).

on Rh(111). The formation of two different well-ordered V-oxide structures $(\sqrt{7} \times \sqrt{7})R19.1°$ and $(\sqrt{13} \times \sqrt{13})R13.8°$ in the submonolayer regime with identical electronic and vibrational signatures, as a result of two different preparation procedures, emphasizes the importance of the kinetics in ultrathin oxide film growth. The kinetic route is determined by the substrate temperature, the oxygen partial pressure, and the preparation procedure (reactive evaporation or postoxidation). For V-oxide films prepared by postoxidation metallic vanadium is first evaporated onto the clean Rh(111) surface at room temperature, which results in a pseudomorphic growth of mainly 2D vanadium islands,[35] indicative of strong interaction between Rh and V. This V/Rh(111) surface is afterwards exposed to oxygen, which leads to a breaking of the V-Rh bonds and the formation of a V oxide. In the reactive evaporation procedure the Rh(111) surface is oxygen predosed prior to the V evaporation, which results in the formation of a dense chemisorbed oxygen Rh(111)-(2×1)-O layer, onto which vanadium atoms and/or VOx clusters (oxidized in the O_2 atmosphere) are deposited. Thus the initial conditions for film growth are different for the two cases considered and consequently lead to different oxide structures in the submonolayer coverage range, the $\sqrt{7}$ or the $\sqrt{13}$ structure. However, both preparation procedures are equally efficient in oxidizing the V metal, since both structures have the same oxidation state, as indicated by XPS.

It is interesting to compare the V-oxide structures formed at submonolayer coverages on Rh(111) and Pd(111) surfaces. On Pd(111), (4×4) and (2×2) phases with formal stoichiometries of V_5O_{14} and V_2O_3, respectively, were found experimentally and understood theoretically by DFT calculations.[4–6] These phases exist only for submonolayer oxide coverages and therefore represent interface-stabilized structures as compared to the known bulk-type V-oxide phases.[4–6] The situation with vanadium oxide overlayers on Rh(111) seems similar to that on Pd(111), in that the $\sqrt{7}$ and $\sqrt{13}$ structures on Rh(111) may also be considered as interface-mediated oxide phases. They both exhibit a formal stoichiometry of VO$_3$, which is not possible in a bulk form. The reason for this is that a layer of oxygen is present at the metal-oxide interface (see structural models of the $\sqrt{7}$ and $\sqrt{13}$ phases in Fig. 7), which reduces the formal oxidation state of the V atoms in the oxide overlayer to ~5$^+$. Although the $\sqrt{7}$ and $\sqrt{13}$ layers contain vanadyl (V=O) groups [see HREELS spectrum of Fig. 6(d)], which are typical for the V_2O_5 (001) surface,[32,36] the $\sqrt{7}$ and $\sqrt{13}$ phases are clearly distinguished from the orthorhombic structure of the bulk-type V_2O_5 phase.[37] For coverages exceeding the first oxide monolayer (~0.6 MLE) the $\sqrt{7}$ and $\sqrt{13}$ phases collapse. They cannot form multilayers or grow as a 3D bulk

crystal, because the second oxide layer is not stabilized by the metal substrate anymore. On Pd(111), the corresponding interface-stabilized structures also cannot grow beyond the monolayer coverage.

In the coverage regime $0.6 < \Theta < 1$ MLE the $\sqrt{7}$ and $\sqrt{13}$ structures are replaced by several phases: the hex-VO$_2$ (Moirè), oblique, and wagon-wheel phases, where the oxidation state of the V atoms progressively decreases from 4^+ to 2^+ with increasing oxide coverage. For $\Theta \sim 1$ MLE the surface is almost fully covered by the wagon-wheel VO phase. This occurs although the sample is kept in oxygen throughout the V deposition and the subsequent cooling in oxygen atmosphere. This peculiar behavior may be understood by considering the following qualitative growth model. For submonolayer oxide coverages oxide-free Rh patches are available at the surface, which are capable of dissociating molecular oxygen and serve as a reservoir of reactive atomic oxygen species for the V atoms hitting the surface. Therefore, oxide structures with high oxidation states (of the order of 5^+) form in the submonolayer regime. At a critical coverage of about 0.6 MLE the surface is fully covered by oxygen-terminated oxide phases and the dosed molecular oxygen cannot dissociate easily anymore. The V atoms deposited can be only oxidized by the oxygen atoms available in the oxide overlayer, a process which leads to the formation of new, but reduced oxide phases. It appears that the molecular O$_2$ from the gas phase is incapable of oxidizing these structures and seems to play no role for the oxide growth in this coverage regime. This mechanism is operative until an oxide coverage of ~ 1 MLE is reached. At this point the oxide film displays the lowest possible oxidation state (2^+) by forming the VO-like wagon-wheel phase. Additional deposited vanadium nucleates in metallic form since the VO phase cannot be further reduced. The metallic vanadium deposits are, however, capable of dissociating the molecular oxygen from the gas phase. Thus, higher oxidized phases can be formed, which will immediately become reduced again by additional vanadium and the growth of a VO crystal might be expected. This would be kinetically favored, but is energetically precluded for two reasons. First, a (111) terminated VO crystal is unstable due to the diverging surface energy for increasing film thickness. For a film thickness exceeding 1 ML the substrate will not anymore efficiently screen the surface dipole (note that the wagon-wheel VO-(111) layer is only stable as a monolayer structure). Second, nonpolar VO terminations, e.g., VO (100), would be unfavorable due to the high lattice misfit to the Rh(111) substrate and the resulting high interfacial energy. These energy contributions (surface and interface energies) can be minimized by growing a bulk-type V$_2$O$_3$ phase on top of the hex-VO$_2$ phase. Indeed, the latter phase reduces the interface energy to the substrate by forming a coincidence structure. Since the hex-VO$_2$ structure is a purely thin-film oxide phase[4] and is not stable in a bulk form, the most favorable continuation of the growth under the present experimental condition is the formation of the bulk V$_2$O$_3$ phase on top of hex-VO$_2$ islands. This parallels the situation for V-oxide films on Pd(111), where similar VO$_2$-type phases in the intermediate coverage regime have been observed.[4,5] The phase separation into oxide structures

with different oxidation states is a natural consequence of the incorporation of additional V atoms into the oxide layer while the additional oxygen uptake of the surface is slow. This is achieved by an adequate balance of the areas of the oblique, hex-VO$_2$, and wagon-wheel phases. A qualitative evaluation of the STM images suggests that the density of the respective oxide structure increases in the sequence oblique $\rightarrow$ wagon-wheel $\rightarrow$ hex-VO$_2$. The mixtures of different structures result in a continuous reduction of the overall oxidation state of the oxide layer, until the 3D oxide growth commences on top of the hex-VO$_2$ at $\Theta \geq 1.2$ MLE.

It is implicitly implied in the above-mentioned mechanism for oxide formation that the evaporated V is not likely to be oxidized in the gas phase. Otherwise, the reduction of the oxide overlayer during further growth is difficult to understand. For thick vanadium oxide layers, the substrate material seems to have little influence on the growing oxide film. V$_2$O$_3$ films with corundum crystal structure have been prepared on Pd(111), Au(111), or W(110) surfaces[5,38,39] under similar preparation conditions. Therefore, for thick oxide layers, bulk V$_2$O$_3$ is the most stable oxide phase under UHV preparation conditions.

V. SUMMARY

The growth of vanadium oxide films on Rh(111) has been studied at the atomic level by STM, LEED, XPS, and HREELS. The V-oxide growth has been followed at 250 °C and 400 °C substrate temperatures. The observed oxide phases are independent of the substrate temperature, but the morphologies are different. For the higher substrate temperature better ordering is observed, due to increased mobility at elevated substrate temperatures. For submonolayer oxide coverages ($\Theta < 0.6$ MLE) two different oxide structures with similar electronic and vibrational signatures have been obtained by choosing different kinetic routes. Reactive evaporation leads to the formation of a $(\sqrt{7} \times \sqrt{7})R19.1°$ structure, whereas postoxidation produces a $(\sqrt{13} \times \sqrt{13})R13.8°$ structure. Both phases represent interface-mediated oxide structures, which are only stable in the submonolayer regime. For oxide coverages in the range $0.6 < \Theta < 1.2$ MLE the $\sqrt{7}$ and $\sqrt{13}$ phases collapse and are replaced by several phases in a narrow coverage range, the hex-VO$_2$, the oblique, and the VO-like wagon-wheel phase. Eventually, for coverages exceeding 2 MLE a bulk-type V$_2$O$_3$ phase with the corundum structure is formed, which grows epitaxially in the form of three-dimensional crystallites. The latter are oriented with the (0001) plane parallel to the Rh(111) surface, with the V$_2$O$_3$(0001) terraces terminated by vanadyl groups.

*Electronic address: svetlozar.surnev@uni-graz.at

[1] F. Chudnovskiy, S. Luryi, and B. Spivak, *Future Trends in Microelectronics: the Nano Millenium* (Wiley Interscience, New York, 2002).

[2] A. Bell, Science **299**, 1688 (2003).

[3] S. Surnev, L. Vitali, M.G. Ramsey, F.P. Netzer, G. Kresse, and J. Hafner, Phys. Rev. B **61**, 13 945 (2000).

[4] S. Surnev, G. Kresse, M.G. Ramsey, and F.P. Netzer, Phys. Rev. Lett. **87**, 086102 (2001).

[5] S. Surnev, G. Kresse, M. Sock, M.G. Ramsey, and F.P. Netzer, Surf. Sci. **495**, 91 (2001).

[6] S. Surnev, M. Sock, G. Kresse, J.N. Andersen, M. Ramsey, and F. Netzer, J. Phys. Chem. B **107**, 4377 (2003).

[7] M. Todorova, W.X. Li, M.V. Ganduglia-Pirovano, C. Stampfl, K. Reuter, and M. Scheffler, Phys. Rev. Lett. **89**, 096103 (2002).

[8] R.J. Madix and J.T. Roberts, *Surface Reactions*, Springer Series in Surface Science Vol. 34 (Springer-Verlag, Berlin, 1994).

[9] M.V. Ganduglia-Pirovano, K. Reuter, and M. Scheffler, Phys. Rev. B **65**, 245426 (2002).

[10] I. Kardinal, F.P. Netzer, and M.G. Ramsey, Surf. Sci. **376**, 229 (1997).

[11] R. Nyholm, J.N. Andersen, U. Johansson, B.N. Jensen, and I. Lindau, Nucl. Instrum. Methods Phys. Res. A **520**, 467 (2001).

[12] S. Donijac and M. Sunjic, J. Phys. C **3**, 285 (1970).

[13] G. Kresse and J. Furthmüller, Comput. Mater. Sci. **6**, 15 (1996).

[14] G. Kresse and D. Joubert, Phys. Rev. B **59**, 1758 (1999).

[15] J.P. Perdew, J.A. Chevary, S.H. Vosko, K.A. Jackson, M.R. Pederson, D.J. Singh, and C. Fiolhais, Phys. Rev. B **46**, 6671 (1992).

[16] G. Kresse, S. Surnev, M.G. Ramsey, and F.P. Netzer, Surf. Sci. **492**, 329 (2001).

[17] J. Tersoff and D.R. Hamann, Phys. Rev. B **81**, 805 (1985).

[18] R. Roy, R. Guo, A.S. Blaha, and L.E. Cross, J. Vac. Sci. Technol. A **12**, 269 (1994).

[19] G.A. Sawatzky and D. Post, Phys. Rev. B **20**, 1546 (1979).

[20] R. Zimmermann, P. Steiner, R. Claessen, F. Reinert, S. Hüfner, P. Blaha, and P. Dufek, J. Phys.: Condens. Matter **11**, 1657 (1999).

[21] S. Schwegmann, H. Over, V.D. Renzi, and G. Ertl, Surf. Sci. **375**, 91 (1997).

[22] F.P. Netzer, Surf. Rev. Lett. **9**, 1553 (2002).

[23] C. Klein, G. Kresse, S. Surnev, F.P. Netzer, M. Schmid, and P. Varga, Phys. Rev. B **68**, 235416 (2003).

[24] J. Schoiswohl, M. Sock, G. Kresse, M.G. Ramsey, and F.P. Netzer (unpublished).

[25] S. Surnev, J. Schoiswohl, G. Kresse, M.G. Ramsey, and F.P. Netzer, Phys. Rev. Lett. **89**, 246101 (2002).

[26] R.A. Bennet, C.L. Pang, N. Pertkins, R.D. Smith, P. Morrall, R.I. Kvon, and M. Bowker, J. Phys. Chem. B **106**, 4688 (2002).

[27] L. Zhang, J. van Ek, and U. Diebold, Phys. Rev. B **59**, 5837 (1999).

[28] P.W. Tasker, J. Phys. C **12**, 4977 (1979).

[29] W. Ranke, M. Ritter, and W. Weiss, Phys. Rev. B **60**, 1527 (1999).

[30] M. Ritter, W. Ranke, and W. Weiss, Phys. Rev. B **57**, 7240 (1999).

[31] T.E. Norwood and J.L. Fry, Phys. Rev. B **2**, 472 (1970).

[32] H. Poelman, J. Vennik, and G. Dalmai, J. Electron Spectrosc. Relat. Phenom. **44**, 251 (1987).

[33] N. Magg, J.B. Giorgi, T. Schroeder, M. Bäumer, and H.J. Freund, J. Phys. Chem. B **106**, 8756 (2002).

[34] A.-C. Dupuis, M.A. Haija, B. Richter, H. Kuhlenbeck, and H.J. Freund, Surf. Sci. **539**, 99 (2003).

[35] C. Konvicka, W. Rupp, M. Schmid, and P. Varga (private communication).

[36] B. Tepper, B. Richter, A.-C. Dupuis, H. Kuhlenbeck, C. Hucho, P. Schilbe, M.A. bin Yarmo, and H.J. Freund, Surf. Sci. **64**, 496 (2002).

[37] J. Haber, M. Witko, and R. Tokarz, Appl. Catal., A **157**, 3 (1997).

[38] K.B. Lewis, S.T. Oyama, and G.A. Somorjai, Surf. Sci. **233**, 75 (1990).

[39] A.-C. Dupuis, Ph.D. thesis, Humboldt Universität zu Berlin, 2002.